Title

High Resolution Photoelectron Spectroscopy of the Acetyl Anion

Journal

The Journal of Physical Chemistry A, 126(43)

ISSN

1089-5639

Authors

DeWitt, Martin

Babin, Mark C

Lau, Jascha A

et al.

Publication Date

2022-11-03

DOI

10.1021/acs.jpca.2c06214

High Resolution Photoelectron Spectroscopy of the Acetyl Anion

Martin DeWitt,[a] Mark C. Babin,[a,c] Jascha A. Lau,[a] Tonia Solomis,[a] Daniel M. Neumark[a,b]*

[a] *Department of Chemistry, University of California, Berkeley, CA 94720, USA*

[b] *Chemical Sciences Division, Lawrence Berkeley National Laboratory, Berkeley, CA 94720, USA*

Corresponding Author

* dneumark@berkeley.edu

ABSTRACT

High-resolution photoelectron spectra of cryogenically cooled acetyl anions (CH_3CO^-) obtained using slow photoelectron velocity-map imaging are reported. The high resolution of the photoelectron spectrum yields a refined electron affinity of 0.4352 ± 0.0012 eV for the acetyl radical as well as the observation of new vibronic structure that is assigned based on *ab initio* calculations. Three vibrational frequencies of the neutral radical are measured to be 1047 ± 3 cm^{-1} (ν_6), 834 ± 2 cm^{-1} (ν_7), and 471 ± 1 cm^{-1} (ν_8). This work represents the first experimental measurement of the ν_6 frequency of the neutral. The measured electron affinity is used to calculate a refined value of 1641.35 ± 0.42 kJ mol^{-1} for the gas-phase acidity of acetaldehyde. Analysis of the photoelectron angular distributions provides insight into the character of the highest occupied molecular orbital of the anion, revealing a molecular orbital with strong *d*-character. Additionally, details of a new centroiding algorithm based on finite differences, which has the potential to decrease data acquisition times by an order of magnitude at no cost to accuracy, are provided.

I. Introduction

The acetyl radical (CH_3CO) has been studied extensively due to its relevance to the combustion of biofuels and biofuel surrogates,[1-2] as well as atmospheric chemistry.[3-7] There are several pathways that lead to the formation of CH_3CO in the atmosphere, including the reaction of acetaldehyde (CH_3CHO) with OH[3] and the UV photolysis of acetone (CH_3COCH_3).[5-6] Following its formation in the atmosphere, the acetyl radical plays a key role in the formation of the peroxyacetyl nitrate ($CH_3C(O)O_2NO_2$), which is an important reservoir for NO and NO_2.[8] The acetyl radical has also been found to be a product of UV photolysis of pyruvic acid, an α-keto carboxylic acid that is abundant in secondary organic aerosols and is a necessary part of many metabolic processes.[9-10]

The importance of the acetyl radical to these processes has motivated a number of spectroscopic studies on its reactivity and structure.[5, 11-19] It was first spectroscopically observed by Morton and Falconer through electron paramagnetic resonance.[11] Later, Bennett *et al.*[13] used electron spin resonance to show the

unpaired electron was located mostly on the carbonyl carbon atom, but appreciable spin density was located on the adjacent atoms. The photoelectron spectrum of the anion was measured by Nimlos *et al.*,[16] yielding a partially resolved vibrational progression in the ν_8 CCO bending mode of the radical (490 ± 30 cm^{-1}) and an electron affinity (EA) of 0.423 ± 0.037 eV. Rajakumar *et al.*[5] measured the visible absorption spectrum of CH_3CO using cavity ring-down spectroscopy, finding a broad peak centered near 535 nm with no discernible structure. Infrared absorption spectra of CH_3CO have been measured in an Ar matrix, solid Ar, and solid *para*-H_2.[12, 15, 19] Collectively, this work reveals that the radical and its corresponding anion have equilibrium structures with C_s symmetry. For the radical, the vibrational frequencies of all but one totally symmetric mode (ν_6 CCH bend) and two non-totally symmetric modes (ν_{11} out-of-plane deformation and ν_{12} methyl torsion) have been experimentally determined in Ar and H_2 matrices. Tentative assignments by Das and Lee[19] to an observed band at 1419.9 cm^{-1} as the ν_{10} fundamental have been called into question by Estep *et al.*[20] who argue for a reassignment as the ν_4 fundamental. Experimentally determined heats of formation suggest that the acetyl radical is more stable than its isomeric counterpart, the vinoxy radical CH_2CHO ($\Delta_fH^o_{298}(CH_3CO)$ = -10.28 kJ mol^{-1} vs $\Delta_fH^o_{298}(CH_2CHO)$ = 16.13 kJ mol^{-1}).[21] CH_3CO has been found to serve as an intermediate in the photodissociation of CH_2CHO to CH_3 + CO,[18, 22] which has an experimentally determined barrier height for dissociation of CH_3CO to CH_3 + CO of 0.75 ± 0.02 eV.[14, 17]

In their study of the anion photoelectron spectrum, Nimlos *et al.*[16] combined their electron affinity (0.423 ± 0.037 eV) with the available experimentally determined heat of formation and gas phase acidity of acetaldehyde, -166.1 ± 0.5 kJ mol^{-1} [23] and 1632 ± 8 kJ mol^{-1},[24] respectively, to determine the heat of formation of acetyl to be -22.6 ± 8.8 kJ mol^{-1}. A subsequent study by Fogleman *et al.*[25] using threshold photoelectron-photoion coincidence found a much larger value of -9.8 ± 1.8 kJ mol^{-1}. The discrepancy between the two values can be largely attributed to the uncertainty of the gas-phase acidity of acetaldehyde, which could not be measured directly through reaction kinetics due to the instability of the acetyl anion compared to the isomeric vinoxide anion.[24]

In this work, we report the high-resolution photoelectron spectrum of CH_3CO^- using slow electron velocity-map imaging of cryogenically cooled anions (cryo-SEVI).[26] Cryo-SEVI is a high-resolution variant of photoelectron spectroscopy capable of measuring molecular photodetachment transitions as narrow as 1 cm^{-1} FWHM that report on the vibronic nature of the corresponding neutral.[27-28] A tunable IR OPO/OPA was recently integrated into the experimental apparatus, enabling efficient cryo-SEVI investigations of anions with detachment energies in the infrared, such as the acetyl anion, as well as studies of the effect of vibrational pre-excitation on the cryo-SEVI spectra, as has been previously reported.[28] The cryo-SEVI spectrum of the acetyl anion is considerably better resolved than the previous photoelectron spectrum,[16] yielding numerous vibrational frequencies and a refined electron affinity of the corresponding

radical that is used to calculate an improved value for the gas-phase acidity of acetaldehyde. We also detail a new data analysis algorithm for our photoelectron images, which was used to detect and centroid photoelectrons for all the presented cryo-SEVI spectra at a fraction of the data collection times typical for this experiment.

II. Experimental Methods

The cryo-SEVI method has been described in detail previously.[26-27, 29] Here, acetyl anions were prepared by expanding a gas mixture of trace NF_3 and $CH_3COSi(CH_3)_3$ in He through an Even-Lavie pulsed valve coupled to a filament ionizer.[30] Fluoride ions are generated *via* dissociative electron attachment to NF_3 and serve to preferentially break the C-Si bond in $CH_3COSi(CH_3)_3$, leaving behind the acetyl anion (CH_3CO^-). The anions pass through a series of ion optics including a skimmer held at a repulsive voltage, a collimating radiofrequency (RF) hexapole, and a mass-selecting RF quadrupole, before entering a RF octupole ion trap held at 5 K. Ions spend ~40 ms in the trap, where they are cooled to roughly 10 K *via* collisions with helium buffer gas[26] before being extracted from the trap into a Wiley-McLaren mass spectrometer.[31] After traveling along a perpendicular time-of-flight path, the ions of interest are photodetached inside a seven-plate VMI spectrometer by a pulsed laser beam.[27, 32] As discussed previously,[26-27, 29] the resolution of cryo-SEVI is best for slow electrons, so it is advantageous to photodetach near the electron affinity of the neutral. Owing to the low electron affinity (< 0.5 eV) of the acetyl radical, tunable light in the mid-infrared region is needed to accomplish this. Hence, acetyl anions were detached using a tabletop OPO/OPA (LaserVision) pumped with the fundamental from a Nd:YAG laser (Continuum SureLite EX) running at 10 Hz, which can produce tunable light in the near- and mid-infrared from 710 nm to 880 nm (1.75 eV to 1.41 eV) as well as from 1.3 μm to 16 μm (0.95 eV to 0.077 eV).[33]

Photoelectrons are analyzed with a position-sensitive detector comprising two chevron-stacked microchannel plates coupled to a phosphor screen.[34] A CCD camera takes a 768 × 768 pixel image of the phosphor screen each experimental cycle, and the electron spots are event-counted, centroided, and binned into a 1024 × 1024 pixel grid.[35] New additions to the event-counting and centroiding algorithm that enable centroid analysis of overlapping electron spots, thereby improving the rate of data collection, are outlined below. Photoelectron centroids are accumulated over several thousand experimental cycles into a single velocity-mapped image, and the radial and angular distributions of the images are calculated using the Maximum Entropy Velocity Legendre Reconstruction (MEVELER) method.[36] The electron kinetic energy (eKE) distributions are related to the radial distributions by acquiring images of the well characterized photodetachment transitions of O^- at several different photon energies.[37]

Since the VMI spectrometer has a roughly constant resolving power (ΔeKE/eKE), photoelectrons with lower kinetic energies are measured with higher resolution.[27, 32] For this reason, cryo-SEVI spectra are acquired by first taking an overview spectrum at a relatively high detachment energy and taking subsequent spectra at detachment energies slightly above the features of interest. Narrow high-resolution windows of these spectra are concatenated to create one high-resolution photoelectron spectrum. Cryo-SEVI spectra are plotted as a function of electron binding energy (eBE), determined by eBE = hν – eKE.

In addition to eKE distributions, VMI gives information about the angular distribution of the detached photoelectrons (PAD) for each transition. For single-photon detachment using linearly polarized light, the PAD is given by[38]

$$\frac{d\sigma}{d\Omega} = \frac{\sigma_{tot}}{4\pi}\left(1 + \beta P_2(\cos\theta)\right) \quad (1)$$

where σ_{tot} is the total photodetachment cross-section, $P_2(x)$ is the second order Legendre polynomial, θ is the angle of the photoelectron velocity vector relative to the laser polarization axis, and β is the anisotropy parameter, which ranges between -1 for perpendicular and +2 for parallel detachment. The variation of the anisotropy parameter as a function of eKE reflects the symmetry and angular momentum of the orbital from which the electron is detached.

New Data Analysis Algorithm

When detected by the CCD camera, each electron spot on the phosphor screen covers an area wider than a single pixel, usually about 5 - 10 pixels (px) wide. These spots are typically brightest in the center with a roughly Gaussian shape, which means the spot centroids can be calculated to a precision much greater than the size of the spot. As cryo-SEVI is a technique focused on achieving maximal resolution, it is desirable to accumulate the centroids of the photoelectrons rather than accumulating the electron spots themselves in order to collect images with the narrowest possible features. One of the first implementations of centroiding in ion imaging experiments was by Houston and coworkers,[39] who used a simple and fast algorithm which identified pixels above a specified intensity that were brighter than the four immediately neighboring pixels. Owing to the ever-increasing computational power of modern computers, more complex algorithms can be implemented that can process images in real time to calculate electron centroids with subpixel precision.

The NuACQ software[35] developed in the Suits group analyzes each camera frame using a connected component labeling (CCL) algorithm, which identifies regions of pixels with intensity above some fixed threshold value as individual electron spots. The centroids of these spots are then taken to be the intensity-weighted center of mass (CoM) of each region

$$(X_{CoM}, Y_{CoM}) = \left(\frac{\sum X_i I_i}{\sum I_i}, \frac{\sum Y_i I_i}{\sum I_i} \right) \tag{2}$$

where X_i, Y_i are the Cartesian coordinates and I_i is the intensity of the i^{th} pixel. This method, which will henceforth be referred to as the CoM method, has been shown to give subpixel resolution, allowing for the collection of high resolution VMI images even with low resolution cameras. However, if two electrons impact the detector in proximity of one another such that their images on the camera overlap, the CCL algorithm will not be able to distinguish the two. The combined CoM centroid of the overlapping electron spots will be calculated and binned, leading to blurring of the resulting accumulated VMI image. The NuACQ software prevents this blurring effect by simply discarding any regions with too high of pixel count, which are assumed to be overlapping spots. Additionally, photoelectrons are collected at a sufficiently low count rate to limit the number of overlapping spots. However, this procedure not only lengthens the accumulation time of each VMI image, but also can alter the data for photoelectrons with lower kinetic energies as these strike the detector at smaller radial distances. They are therefore more likely to overlap with other electrons and be discarded.

To avoid this artificial distortion, the centroiding algorithm used in our lab has been improved to facilitate the calculation of virtually all imaged electron spots, regardless of their proximity to one another. The initial steps of the algorithm are the same as in the NuACQ software: identify regions of neighboring lit pixels using the CCL algorithm and calculate the CoM centroid for small regions (typically < 120 px in size). For large regions, which are assumed to comprise multiple electron spots, the numerical gradient of the intensity along the *x* and *y* Cartesian axes is analyzed to find local maxima in the intensity. If a pixel (*X,Y*) in the region is found to be a local maximum along both Cartesian axes, it is treated as the center of one of the spots composing the region. In order to achieve sub-pixel resolution, the gradient around the pixel (*X,Y*) along each axis is approximated as a line with a root that is considered to be the centroid of the spot, calculated by

$$(X_{Center}, Y_{Center}) = \left(X + \frac{\left.\frac{\partial I}{\partial x}\right|_{X,Y}}{\left.\frac{\partial I}{\partial x}\right|_{X,Y} - \left.\frac{\partial I}{\partial x}\right|_{X+1,Y}}, Y + \frac{\left.\frac{\partial I}{\partial y}\right|_{X,Y}}{\left.\frac{\partial I}{\partial y}\right|_{X,Y} - \left.\frac{\partial I}{\partial y}\right|_{X,Y+1}} \right) \tag{3}$$

where *X* and *Y* are the Cartesian coordinates and $\left.\frac{\partial I}{\partial x(y)}\right|_{X,Y}$ is the central finite difference along *x* (or *y*) evaluated at the point *X,Y*. For the sake of clarity, we will refer to this improved centroiding algorithm as the hybrid gradient-CoM (HGCM) method. Occasionally the HGCM algorithm may calculate two nearby centroids for the same electron spot; this can be resolved by taking an average of any two centroids found within 1.5 px of each other, weighted by the intensities of the pixel encapsulating each centroid. Fig. 1a

shows a representative electron spot typical for cryo-SEVI measurements, while Fig. 1b shows a lineout of the intensity of that spot and how the root of the derivative of the intensity closely approximates the spot center. Fig. 1c shows a small section of a camera frame with multiple electron spots to demonstrate the efficacy of the new HGCM centroiding method. The regions found with the CCL algorithm are bordered in gray, and the CoM centroids of the three regions with sufficiently low pixel count are represented with red dots. The large region, whose CoM centroid is shown as a red X, would previously have been discarded, but is instead treated with the gradient method with centroids represented as blue dots. In this small example, half of the electron spots identified with the HGCM method would have been discarded with the previously used CoM method.

Benchmark tests of simulated images show the average RMS error of the CoM method on small (non-overlapping) spots to be around 0.01 px for a 768 × 768 pixel grid, while the average error of HGCM method on large (overlapping) spots is around 0.1 px. While this error is an order of magnitude larger than the CoM method, it is still smaller than the pores of the MCPs used in our VMI spectrometer (25 μm pore diameter, corresponding to ~0.3 px), meaning that the experimental resolution remains hardware limited. Additionally, despite the increase in computational cost associated with the HGCM method, the computer used (Dell Z240, Intel i5 3.2 GHz processor, 8 GB RAM) can process and centroid each image in ≤ 5 ms, well below the 50 ms between experimental cycles that are typical for cryo-SEVI.

Perhaps the largest benefit from this new algorithm is the drastic decrease in data acquisition time. Previously, the number of detached electrons per laser shot was held down to minimize the amount of overlapping electron spots in each image, typically between 10 and 50 electrons per image. Following implementation of the HGCM method, however, photoelectron images containing between 100 and 300 electrons can be collected and processed without loss of resolution. The data presented in this work were processed simultaneously using the old centroiding method as well as the described new method to compare the two methods at a detachment rate of around 100 electrons per laser shot. On average, the CoM method was only able to identify 2/3 as many electrons as the new centroiding method. Tests at detachment rates greater than 200 electrons per laser shot showed that the CoM method was not able to identify even half as many electrons as the new method. The improved collection efficiency combined with the ability to collect data at higher detachment rates thereby increases our data acquisition rate by as much as an order of magnitude.

III. Computational Methods

To facilitate assignment of the experimental spectral features, electronic structure calculations were carried out for the ground states of both the acetyl anion and neutral radical using density functional theory.

The equilibrium geometries and harmonic frequencies of both species, given in Tables S1, S2, and S3 in the supplemental material, were calculated with the ωB97X-2(LP) functional[40] and 6-311+G* basis set[41] using version 5.4 of the QChem software package.[42] Other density functionals were tested, such as B3LYP,[43-44] but the ωB97X-2(LP) functional provided neutral harmonic frequencies that most closely matched the experimental values. Comparison of the neutral harmonic frequencies calculated using different levels of theory is given in Table S4 of the supplemental material. The equilibrium geometries, harmonic frequencies, and normal modes were used to calculate the Franck-Condon (FC) profile of the $\tilde{X}^2A' \leftarrow \tilde{X}^1A'$ detachment transition of CH_3CO^- using version 1.1 of the ezFCF software package.[45] All vibrational modes were treated within the harmonic approximation, and full Duschinsky mixing was invoked to account for differences between the anion and neutral normal modes when calculating the FC overlap integrals.[46]

IV. Results

The cryo-SEVI spectrum of the $\tilde{X}^2A' \leftarrow \tilde{X}^1A'$ photodetachment transition of CH_3CO^- is shown in Fig. 2. The blue trace is an overview spectrum taken at a high photon energy while the black traces are high-resolution windows taken at photon energies just above various features of interest and scaled to match the intensities in the overview spectrum. Simulated FC profiles (Section V) are depicted as red sticks and facilitate the assignment of each experimentally observed feature as shown in Table 1.

The first peak in the cryo-SEVI spectrum (peak A) is assigned to the vibrational origin, above which vibrational structure spanning ~5000 cm^{-1} in eBE is resolved. The overview spectrum (blue) shows an extended progression of features with a frequency of 470 cm^{-1}, in agreement with the previous photoelectron study by Nimlos *et al*.[16] but with improved resolution. In the high-resolution spectra (black), each peak in the overview starting with peak D is further resolved, showing two lower intensity peaks on either side. Peak positions and assignments (see Discussion) are listed in Table 1, with uncertainty values shown in parentheses corresponding to one standard deviation of a Gaussian function fit to the experimental features. Experimental parameters obtained for the acetyl radical, extrapolated from the cryo-SEVI spectrum, are given in Table 2 along with comparison to previously reported values.

From the PAD as revealed by the photoelectron images, the anisotropy parameter, β, of peaks A and B was determined at various photon energies as depicted in Fig. 3, which shows the dependence of the anisotropy parameter on eKE. At large eKE, these values approach the $\beta = 2$ limit, which is a signature of *p*-wave detachment ($l = 1$, the orbital angular momentum of the ejected electron). The PAD is consistent with the observation that the signal for each peak drops considerably at low eKE, according to the Wigner threshold law[47] when $l = 1$:

$$\sigma \propto (eKE)^{l+1/2} \quad (4)$$

As discussed in previous work,[48-49] p-wave detachment limits the resolution of our experiment, and the narrowest peaks observed here have a full width at half maximum of 21 cm^{-1}. Further interpretations of the PAD and insights into the molecular orbital from which photodetachment occurs will be discussed in Section V.

V. Discussion

Assignment of Features

The ωB97X-2(LP)/6-311+G* Franck-Condon simulation is in good agreement with the cryo-SEVI spectrum, facilitating assignments for all features as transitions to Franck-Condon allowed vibrational states in the neutral. As mentioned in the previous section, the first peak in the spectrum, at 3511 cm^{-1} (peak A), is assigned to the vibrational origin, leading to a value of 0.4352 ± 0.0012 eV for the adiabatic electron affinity (EA) of CH_3CO. This value is in good agreement with the previously measured value of 0.432 ± 0.037 eV by Nimlos *et al*.[16] The dominant progression (B-D-G-J-M-P-S-U-V-W-X) has an average spacing of 470 cm^{-1}, in good agreement with the previously reported value of 468.1 cm^{-1} for the ν_8 CCO bending mode measured in solid *para*-H_2.[19] The high Franck-Condon activity of the CCO bending mode indicates a large change in CCO bond angle upon photodetachment, which is consistent with our calculated values of 112.9º and 128.4º in the anion and neutral, respectively. Notably, some intensity in the higher eBE features in this progression may arise from combination band transitions involving the ν_8 and ν_3 (CO stretch) modes, which gain appreciable intensity in the FC simulation after 5800 cm^{-1} (peak M). Das and Lee found the ν_3 frequency to be 1880 cm^{-1}, which is almost exactly four times the value we measure for the ν_8 frequency, leading to the $3_0^1 8_0^n$ transitions appearing at nearly identical energies to the 8_0^{n+4} transitions. Transitions involving the ν_3 mode are also expected to have appreciable FC activity due to a significant change in the CO bond length, from 1.24 Å for the anion to 1.19 Å for the neutral, caused by the detached electron residing mainly in a CO π* orbital. This orbital, the highest occupied molecular orbital (HOMO) of the anion, is shown in Fig. 4.

The lower intensity features that appear in the high-resolution spectra are assigned to vibronic transitions based on comparison to the FC simulation. Peak C is assigned to the 7_0^1 transition, giving a value of 836 ± 14 cm^{-1} for the ν_7 frequency that is in excellent agreement with the previously reported value of 836.6 cm^{-1} by Das and Lee.[19] The progression of features that appear left of the main progression (F-I-L-O-R) comprises $7_0^1 8_0^n$ combination bands. Peak E in Fig. 2 corresponds to the 6_0^1 transition, involving the previously unobserved ν_6 CCH deformation mode. The position of this feature yields the ν_6 frequency of 1045 ± 9 cm^{-1}. It should be noted that while a peak appeared in the high-resolution spectra at 5400 cm^{-1},

corresponding to the 6_0^2 transition, the signal to noise ratio in this spectral region precludes a definitive assignment. The features that appear to the right of the main progression (H-K-N-Q-T) are attributed to $6_0^1 8_0^n$ combination bands.

The extended progression in the ν_8 mode facilitates determination of its effective anharmonicity by performing a weighted least-squares fitting of the transition energies for each feature in the progression, whose values were taken from the highest resolution features measured for each transition, to a power series

$$E_{\mathrm{v}} = \omega_e \left(\mathrm{v} + \frac{1}{2}\right) - \omega_e \chi_e \left(\mathrm{v} + \frac{1}{2}\right)^2 \quad (5)$$

Doing so yields a harmonic frequency ω_e = 470 ± 1 cm^{-1} and an anharmonic correction term $\omega_e\chi_e$ = -0.1 ± 0.2 cm^{-1}. The value for the anharmonic term is thus negligible within error bars, indicating that the bending mode can be described well as a simple harmonic oscillator. The value for the harmonic frequency is in good agreement with the previously measured frequency of 468.1 cm^{-1} by Das and Lee *via* FTIR of the acetyl radical in solid *para*-H_2.[19]

Assuming the ν_8 mode can be treated as a harmonic oscillator, we apply a global fit of the peak energies in the cryo-SEVI spectrum to the following equation to extract refined values for the ν_6, ν_7, and ν_8 modes:

$$E_{\mathrm{shift}} = \omega_6 \mathrm{v}_6 + \omega_7 \mathrm{v}_7 + \omega_8 \mathrm{v}_8 \quad (6)$$

where E_{shift} is the energy difference (in cm^{-1}) between each peak and the vibrational origin, ω_6, ω_7, and ω_8 are the harmonic frequencies of the three modes, and v_6, v_7, and v_8 are the vibrational quanta in each mode (v_6 and v_7 = 0,1 and v_8 ranges from 0 to 8). The weighted least-squares fitting to this model results in the following frequencies for each mode: 1047 ± 3 cm^{-1} for ν_6, 834 ± 2 cm^{-1} for ν_7, and 471 ± 1 cm^{-1} for ν_8. The vibrational frequencies and electron affinity of the acetyl radical extracted from this work are presented in Table 2 and compared to *ab initio* calculations as well as previously reported values.

Determination of Acetaldehyde Gas-phase Acidity

The disparity between the heat of formation of acetyl reported by Nimlos *et al.* (-22.6 ± 8.8 kJ mol^{-1})[16] and that reported by Fogleman *et al.* (-9.8 ± 1.8 kJ mol^{-1})[25] can be largely attributed to the uncertainty in the measurement of the gas-phase acidity of acetaldehyde. Fogleman questioned the electron affinity of acetyl reported by Nimlos based on the difficulty identifying the adiabatic onset from hot bands in their photoelectron spectrum, arguing the electron affinity could instead be 0.481 ± 0.037 eV.[25] However, the value we find for the electron affinity of 0.4352 ± 0.0012 eV shows that Nimlos *et al*. correctly assigned the vibrational origin in their spectrum.. Since the acetyl heat of formation has at this point been

experimentally determined to fairly high precision (-10.28 ± 0.32 kJ mol^{-1})[21], it can be used along with the electron affinity of acetyl to calculate the gas-phase acidity of acetaldehyde by the following relation:

$$\Delta_{acid}H^{\circ}_{298}(\mathrm{CH_3CO\text{-}H}) = \Delta_f H^{\circ}_{298}(\mathrm{CH_3CO}) + \Delta_f H^{\circ}_{298}(\mathrm{H^+}) - \Delta_f H^{\circ}_{298}(\mathrm{CH_3CHO}) - EA(\mathrm{CH_3CO}) \qquad (7)$$

Using the heat of formation values taken from Argonne National Lab's Active Thermochemical Tables (1528.084 kJ mol^{-1} for H^+ and -165.54 ± 0.25 kJ mol^{-1} for CH_3CHO),[21, 50-51] we obtain a value of 1641.35 ± 0.42 kJ mol^{-1} for the gas-phase acidity of acetaldehyde. This value is slightly outside of the error bars of that estimated by DePuy *et al.* (1632 ± 8 kJ mol^{-1}),[24] but the nearly 10 kJ mol^{-1} discrepancy seen here matches the discrepancy between the heats of formation of acetyl reported by Nimlos and by Fogleman, explaining the disparity between their reported values.

Photoelectron Angular Distributions

As can be seen in Fig. 3, the anisotropy parameter β is positive and approaches an asymptotic value of $\beta = 1.75$ at high eKE. For atomic systems, a value of +2 for β indicates photodetachment from an atomic *s* orbital with a photoelectron ejected with pure *p*-wave character (l = 1). To deal with the additional complexity of molecular orbitals (MO), Sanov and coworkers[52] have developed a framework to model PADs of molecular anions by describing the detached molecular orbital as a combination of *s* and *p* orbitals centered on a single atom, and later expanded this model to describe the MO as a linear combination of an arbitrary number of angular momentum components.[53] DeVine *et al.*[54] adapted this to model the HOMO of the pyridinide isomers as combinations of 2*s*, 2*p*, and 3*d* orbitals, i.e. $|\Psi_{spd}\rangle = \sqrt{1-\gamma_1-\gamma_2}|s\rangle + \sqrt{\gamma_1}|p\rangle + \sqrt{\gamma_2}|d\rangle$, which they successfully used to explain the disparity in the PADs of the three isomers. A similar model from Laws *et al.*[55] was independently developed and published soon after. In the mixed-*spd* model, the dependence of the anisotropy parameter on eKE (ε) is given by

$$\beta_{spd}(\varepsilon) = \frac{2\left[\frac{B_1}{A_1}(1-\gamma_1-\gamma_2) - 2\gamma_1 + \frac{A_1}{5B_2}\gamma_2\right]A_2\varepsilon + 2\left(\gamma_1 - \frac{18A_2}{5B_2}\gamma_2\right)A_1A_2\varepsilon^2 + \frac{12A_1}{5B_2}\gamma_2A_2^3\varepsilon^3}{\frac{A_2}{A_1}\gamma_1 + \left[\frac{B_1}{A_1}(1-\gamma_1-\gamma_2) + 2\frac{A_1}{B_2}\gamma_2\right]A_2\varepsilon + 2\gamma_1A_1A_2\varepsilon^2 + 3\gamma_2\frac{A_1}{B_2}A_2^3\varepsilon^3} \qquad (8)$$

Here, A_l, B_l, A_2, and B_2 are the Hanstorp coefficients, where A_l give the relative scaling of the $l \rightarrow l+1$ and $l \rightarrow l-1$ detachment channels and B_l give the relative scaling of the $l-1 \rightarrow l$ and $l \rightarrow l-1$ detachment channels.[53, 56]

The HOMO of the acetyl anion, which is nominally a π* orbital located along the CO bond, is shown in Fig. 4. Since this orbital resembles an atomic *d*-orbital centered between the C and O atoms, the mixed-*spd* model should be able to model the angular dependence of detachment from this orbital. We apply this model in a similar fashion as was performed on the pyridinide isomers.[54] The Hanstorp

coefficients A_1 and B_1 are determined by the effective nuclear charges of the *s* and *p* basis functions Z_0 and Z_1, while A_2 and B_2 are determined by the effective nuclear charges of the *p* and *d* basis functions: Z_1 and Z_2. If we assume the values $A_1 = 0.75$ eV^{-1} and $B_1 = 8A_1/3$, which have been shown to fit well for detachment from a 2*s*-2*p* orbital centered on a carbon atom using both the mixed-*sp* and mixed-*spd* models,[54, 57] the values for Z_0 and Z_1 are then found to both equal 0.885. This leaves only 3 unknown parameters to describe β: Z_2, γ_1, and γ_2. These parameters can be determined from a fit to the experimental PADs. The least squares fit of the mixed-*spd* model to the experimental PAD of acetyl gives $Z_2 = 2.7$, $\gamma_1 = 0.01$, and $\gamma_2 = 0.79$ (and thus $\gamma_0 = 0.2$). The extracted value for Z_2 gives Hanstorp coefficients $A_2 = 0.15$ eV^{-1} and $B_2 = 16.2$ eV^{-1}. The values obtained from the least squares fitting for γ_0, γ_1, and γ_2, which are the contributions from 2*s*, 2*p*, and 3*d* orbitals to the HOMO, respectively, suggest the acetyl anion HOMO is largely *d*-character with some *s*-character and virtually no *p*-character. An electron detached from such an orbital would be in a superposition of mostly $l = 1$ and $l = 3$ partial waves, and would exhibit a poor near-threshold photodetachment cross section,[47] consistent with the observed drop in photodetachment signal at low eKE.

Conclusion

A high-resolution photoelectron spectrum of cryogenically cooled acetyl anions has been obtained using slow photoelectron velocity-map imaging. The work shows an order-of-magnitude improvement in resolution over the previously reported photoelectron spectrum, resulting in newly resolved vibronic structure, a refined value for the electron affinity of the radical, and the experimental determination of the previously unmeasured neutral ν_6 frequency. Additionally, we report the gas phase vibrational frequency for the ν_7 mode for the first time, which had previously only been measured in Ar and H_2 matrices. A new algorithm is also presented, capable of precisely determining the centroids of overlapping electron spots in VMI images and offering a significant decrease in data collection times without sacrificing accuracy. The measured electron affinity was used to calculate the gas-phase acidity of acetaldehyde to a higher precision than earlier studies, which had previously led to uncertainty in the heat of formation of the acetyl radical. The photoelectron angular distribution of acetyl was analyzed by describing the highest occupied molecular orbital of the anion as a linear combination of 2*s*, 2*p*, and 3*d* atomic orbitals with strong d-character.

Acknowledgements

This research was funded by the Director, Office of Basic Energy Sciences, Chemical Sciences Division of the U.S. Department of Energy, under Contract No. DE-AC02-05CH11231, as well as through the Air Force Office of Scientific Research Defense University Research Instrumentation Program under Grant No. FA9550-19-1-0139, DEF. M.C.B. thanks the Army Research Office for a National Defense Science and

Engineering Graduate fellowship. J.A.L thanks the Alexander von Humboldt Foundation for a Feodor Lynen Research Fellowship.

Supporting Information

See supporting information for details regarding calculated geometries and harmonic frequencies given in Tables S1-S4.

[c] *Present Address: Department of Chemistry and Chemical Biology, Harvard University, Cambridge, MA 02138, USA*

References

1. Huynh, L. K.; Violi, A., Thermal Decomposition of Methyl Butanoate: *Ab Initio* Study of a Biodiesel Fuel Surrogate. *J. Org. Chem.* **2008,** *73*, 94-101.
2. Hakka, M. H.; Bennadji, H.; Biet, J.; Yahyaoui, M.; Sirjean, B.; Warth, V.; Coniglio, L.; Herbinet, O.; Glaude, P. A.; Billaud, F.*, et al.*, Oxidation of methyl and ethyl butanoates. *Int. J. Chem. Kinet.* **2010,** *42*, 226-252.
3. Michael, J. V.; Keil, D. G.; Klemm, R. B., Rate constants for the reaction of hydroxyl radicals with acetaldehyde from 244–528 K. *J. Chem. Phys.* **1985,** *83*, 1630-1636.
4. Atkinson, R.; Arey, J., Atmospheric degradation of volatile organic compounds. *Chem. Rev.* **2003,** *103*, 4605-4638.
5. Rajakumar, B.; Flad, J. E.; Gierczak, T.; Ravishankara, A. R.; Burkholder, J. B., Visible Absorption Spectrum of the CH_3CO Radical. *J. Phys. Chem. A* **2007,** *111*, 8950-8958.
6. Rajakumar, B.; Gierczak, T.; Flad, J. F.; Ravishankara, A. R.; Burkholder, J. B., The CH_3CO quantum yield in the 248 nm photolysis of acetone, methyl ethyl ketone, and biacetyl. *J. Photochem. Photobiol. A - Chem.* **2008,** *199*, 336-344.
7. Hu, N.; Green, S. A., Acetyl radical generation in cigarette smoke: Quantification and simulations. *Atmos. Environ.* **2014,** *95*, 142-150.
8. Talukdar, R. K.; Burkholder, J. B.; Schmoltner, A.-M.; Roberts, J. M.; Wilson, R. R.; Ravishankara, A. R., Investigation of the loss processes for peroxyacetyl nitrate in the atmosphere: UV photolysis and reaction with OH. *J. Geophys. Res.* **1995,** *100*, 14163.
9. Sutradhar, S.; Samanta, B. R.; Fernando, R.; Reisler, H., Spectroscopy and Two-Photon Dissociation of Jet-Cooled Pyruvic Acid. *J. Phys. Chem. A* **2019,** *123*, 5906-5917.
10. Guzman, M. I.; Eugene, A. J., Aqueous Photochemistry of 2-Oxocarboxylic Acids: Evidence, Mechanisms, and Atmospheric Impact. *Molecules* **2021,** *26*, 52785278.
11. Morton, J. R.; Falconer, W. E., Electron Paramagnetic Resonance Spectrum of the Acetyl Radical. *Nature* **1963,** *197*, 1103-1103.
12. Shirk, J. S.; Pimentel, G. C., Potential Functions And Bonding in XCO Free Radicals. *J. Am. Chem. Soc.* **1968,** *90*, 3349.
13. Bennett, J. E.; Mile, B.; Ward, B., Electron Spin Resonance Spectrum of Acetyl Radical. *J. Chem. Soc. D* **1969**, 13.

14. Watkins, K. W.; Word, W. W., Addition of methyl radicals to carbon monoxide: Chemically and thermally activated decomposition of acetyl radicals. *Int. J. Chem. Kinet.* **1974,** *6*, 855-873.
15. Jacox, M. E., The Reaction of F^- atoms with Acetaldehyde and Ethylene-oxide - Vibrational-spectra of the CH_3CO and CH_2CHO Free-radicals Trapped in Solid Argon. *Chem. Phys.* **1982,** *69*, 407-422.
16. Nimlos, M. R.; Soderquist, J. A.; Ellison, G. B., Spectroscopy of CH_3CO^- AND CH_3CO. *J. Am. Chem. Soc.* **1989,** *111*, 7675-7681.
17. North, S.; Blank, D. A.; Lee, Y. T., Determination of the Barrier Height to CH_3CO Dissociation. *Chem. Phys. Lett.* **1994,** *224*, 38-42.
18. Osborn, D. L.; Choi, H.; Mordaunt, D. H.; Bise, R. T.; Neumark, D. M.; Rohlfing, C. M., Fast beam photodissociation spectroscopy and dynamics of the vinoxy radical. *J. Chem. Phys.* **1997,** *106*, 3049-3066.
19. Das, P.; Lee, Y. P., Bimolecular reaction of CH_3 + CO in solid p-H_2: Infrared absorption of acetyl radical (CH_3CO) and CH_3-CO complex. *J. Chem. Phys.* **2014,** *140*, 244303.
20. Estep, M. L.; Morgan, W. J.; Winkles, A. T.; Abbott, A. S.; Villegas-Escobar, N.; Mullinax, J. W.; Turner, W. E.; Wang, X.; Turney, J. M.; Schaefer, H. F., Radicals derived from acetaldehyde and vinyl alcohol. *Phys. Chem. Chem. Phys.* **2017,** *19*, 27275-27287.
21. Ruscic, B.; Bross, D. H., Active Thermochemical Tables (ATcT) values based on ver. 1.122r of the Thermochemical Network. ATcT.anl.gov, 2021.
22. Miller, J. L.; McCunn, L. R.; Krisch, M. J.; Butler, L. J.; Shu, J., Dissociation of the ground state vinoxy radical and its photolytic precursor chloroacetaldehyde: Electronic nonadiabaticity and the suppression of the H+ketene channel. *J. Chem. Phys.* **2004,** *121*, 1830-1838.
23. Pedley, J., *Thermochemical data and structures of organic compounds*. CRC Press: 1994; Vol. 1.
24. Depuy, C. H.; Bierbaum, V. M.; Damrauer, R.; Soderquist, J. A., Gas-phase Reactions of the Acetyl Anion. *J. Am. Chem. Soc.* **1985,** *107*, 3385-3386.
25. Fogleman, E. A.; Koizumi, H.; Kercher, J. P.; Sztáray, B.; Baer, T., Heats of Formation of the Acetyl Radical and Ion Obtained by Threshold Photoelectron Photoion Coincidence. *J. Phys. Chem. A* **2004,** *108*, 5288-5294.
26. Hock, C.; Kim, J. B.; Weichman, M. L.; Yacovitch, T. I.; Neumark, D. M., Slow photoelectron velocity-map imaging spectroscopy of cold negative ions. *J. Chem. Phys.* **2012,** *137*, 244201.
27. Weichman, M. L.; DeVine, J. A.; Levine, D. S.; Kim, J. B.; Neumark, D. M., Isomer-specific vibronic structure of the 9-, 1-, and 2-anthracenyl radicals via slow photoelectron velocity-map imaging. *Proc. Natl. Acad. Sci. U. S. A.* **2016,** *113*, 1698-1705.
28. DeWitt, M.; Babin, M. C.; Neumark, D. M., High-Resolution Photoelectron Spectroscopy of Vibrationally Excited OH^-. *J. Phys. Chem. A* **2021,** *125*, 7260-7265.
29. Osterwalder, A.; Nee, M. J.; Zhou, J.; Neumark, D. M., High resolution photodetachment spectroscopy of negative ions via slow photoelectron imaging. *J. Chem. Phys.* **2004,** *121*, 6317-6322.
30. Even, U.; Jortner, J.; Noy, D.; Lavie, N.; Cossart-Magos, C., Cooling of large molecules below 1 K and He clusters formation. *J. Chem. Phys.* **2000,** *112*, 8068-8071.
31. Wiley, W. C.; McLaren, I. H., Time-of-Flight Mass Spectrometer with Improved Resolution. *Rev. Sci. Instrum.* **1955,** *26*, 1150-1157.

32. Eppink, A.; Parker, D. H., Velocity map imaging of ions and electrons using electrostatic lenses: Application in photoelectron and photofragment ion imaging of molecular oxygen. *Rev. Sci. Instrum.* **1997,** *68*, 3477-3484.
33. Bosenberg, W. R.; Guyer, D. R., Broadly Tunable, Single-frequency Optical Parametric Frequency-conversion System. *J. Opt. Soc. Am. B - Opt. Phys.* **1993,** *10*, 1716-1722.
34. Chandler, D. W.; Houston, P. L., Two-dimensional Imaging of State-selected Photodissociation Products Detected by Multiphoton Ionization. *J. Chem. Phys.* **1987,** *87*, 1445-1447.
35. Doyle, M. B.; Abeyasera, C.; Suits, A. G. NuACQ. http://faculty.missouri.edu/suitsa/NuAqc.html.
36. Dick, B., Inverting ion images without Abel inversion: maximum entropy reconstruction of velocity maps. *Phys. Chem. Chem. Phys.* **2014,** *16*, 570-580.
37. Blondel, C.; Chaibi, W.; Delsart, C.; Drag, C.; Goldfarb, F.; Kroger, S., The electron affinities of O, Si, and S revisited with the photodetachment microscope. *Eur. Phys. J. D* **2005,** *33*, 335-342.
38. Cooper, J.; Zare, R. N., Angular Distribution of Photoelectrons. *J. Chem. Phys.* **1968,** *48*, 942-943.
39. Chang, B.-Y.; Hoetzlein, R. C.; Mueller, J. A.; Geiser, J. D.; Houston, P. L., Improved two-dimensional product imaging: The real-time ion-counting method. *Rev. Sci. Instrum.* **1998,** *69*, 1665-1670.
40. Chai, J.-D.; Head-Gordon, M., Long-range corrected double-hybrid density functionals. *J. Chem. Phys.* **2009,** *131*, 174105.
41. Glendening, E. D.; Feller, D., Cation-Water Interactions: The $M^+(H_2O)_n$ Clusters for Alkali Metals, M = Li, Na, K, Rb, and Cs. *J. Phys. Chem.* **1995,** *99*, 3060-3067.
42. Epifanovsky, E.; Gilbert, A. T. B.; Feng, X.; Lee, J.; Mao, Y.; Mardirossian, N.; Pokhilko, P.; White, A. F.; Coons, M. P.; Dempwolff, A. L.*, et al.*, Software for the frontiers of quantum chemistry: An overview of developments in the Q-Chem 5 package. *J. Chem. Phys.* **2021,** *155*, 084801.
43. Becke, A. D., Density-functional thermochemistry. III. The role of exact exchange. *J. Chem. Phys.* **1993,** *98*, 5648-5652.
44. Stephens, P. J.; Devlin, F. J.; Chabalowski, C. F.; Frisch, M. J., *Ab initio* calculation of vibrational absorption and circular dichroism spectra using density functional force fields. *J. Phys. Chem.* **1994,** *98*, 11623-11627.
45. Gozem, S.; Krylov, A. I., The *ezSpectra* suite: An easy-to-use toolkit for spectroscopy modeling. *Wiley Interdiscip. Rev.: Comput. Mol. Sci.* **2022,** *12*.
46. Duschinsky, F., The importance of the electron spectrum in multi atomic molecules. Concerning the Franck-Condon principle. *Acta Physicochim. URSS* **1937,** *7*, 551-566.
47. Wigner, E. P., On the Behavior of Cross Sections Near Thresholds. *Phys. Rev.* **1948,** *73*, 1002-1009.
48. Babin, M. C.; DeVine, J. A.; Weichman, M. L.; Neumark, D. M., Slow photoelectron velocity-map imaging of cold C_7^- and C_9^-. *J. Chem. Phys.* **2018,** *149*, 174306.
49. Babin, M. C.; DeVine, J. A.; DeWitt, M.; Stanton, J. F.; Neumark, D. M., High-Resolution Photoelectron Spectroscopy of Cryogenically Cooled NO_3^-. *J. Phys. Chem. Lett.* **2019,** *11*, 395-400.

50. Ruscic, B.; Pinzon, R. E.; Morton, M. L.; Von Laszevski, G.; Bittner, S. J.; Nijsure, S. G.; Amin, K. A.; Minkoff, M.; Wagner, A. F., Introduction to Active Thermochemical Tables: Several "Key" Enthalpies of Formation Revisited. *J. Phys. Chem. A* **2004,** *108*, 9979-9997.
51. Ruscic, B.; Pinzon, R. E.; Von Laszevski, G.; Kodeboyina, D.; Burcat, A.; Leahy, D.; Montoya, D.; Wagner, A. F., Active Thermochemical Tables: thermochemistry for the 21st century. *J. Phys. Conf. Ser.* **2005**, 561-570.
52. Grumbling, E. R.; Sanov, A., Photoelectron angular distributions in negative-ion photodetachment from mixed sp states. *J. Chem. Phys.* **2011,** *135*, 164302.
53. Khuseynov, D.; Blackstone, C. C.; Culberson, L. M.; Sanov, A., Photoelectron angular distributions for states of any mixed character: An experiment-friendly model for atomic, molecular, and cluster anions. *J. Chem. Phys.* **2014,** *141*, 124312.
54. Devine, J. A.; Babin, M. C.; Blackford, K.; Neumark, D. M., High-resolution photoelectron spectroscopy of the pyridinide isomers. *J. Chem. Phys.* **2019,** *151*, 064302.
55. Laws, B.; Cavanagh, S.; Lewis, B.; Gibson, S., Wigner Near-Threshold Effects in the Photoelectron Angular Distribution of NO_2^-. *J. Phys. Chem. A* **2019,** *123*, 10418-10425.
56. Hanstorp, D.; Bengtsson, C.; Larson, D. J., Angular distributions in photodetachment from O^-. *Phys. Rev. A* **1989,** *40*, 670-675.
57. Culberson, L. M.; Blackstone, C. C.; Wallace, A. A.; Sanov, A., Aromatic Stabilization and Hybridization Trends in Photoelectron Imaging of Heterocyclic Radicals and Anions. *J. Phys. Chem. A* **2015,** *119*, 9770-9777.

TABLE 1. Peak positions, shifts from the vibrational origin, and assignments for detachment transitions for the cryo-SEVI spectrum of the $\tilde{X}^2A' \leftarrow \tilde{X}^1A'$ photodetachment of acetyl in Figure 1. All values are reported in cm^{-1} and uncertainties in peak positions correspond to one standard deviation obtained from a Gaussian fit to the high-resolution scan of the experimental peak.

Label	eBE	Shift	Assignment
A	3511(9)	0	0_0^0
B	3979(13)	468	8_0^1
C	4347(14)	836	7_0^1
D	4444(12)	933	8_0^2
E	4556(9)	1045	6_0^1
F	4816(16)	1305	$8_0^1 7_0^1$
G	4916(13)	1406	8_0^3
H	5025(14)	1515	$8_0^1 6_0^1$
I	5279(14)	1768	$8_0^2 7_0^1$
J	5392(17)	1881	8_0^4
K	5494(36)	1984	$8_0^2 6_0^1$
L	5743(25)	2232	$8_0^3 7_0^1$
M	5863(19)	2352	8_0^5
N	5957(28)	2446	$8_0^3 6_0^1$
O	6227(10)	2716	$8_0^4 7_0^1$
P	6329(14)	2819	8_0^6
Q	6453(31)	2943	$8_0^4 6_0^1$
R	6697(31)	3186	$8_0^5 7_0^1$
S	6797(27)	3287	8_0^7
T	6904(23)	3393	$8_0^5 6_0^1$
U	7280(132)	3769	8_0^8
V	7728(96)	4217	8_0^9
W	8228(97)	4717	8_0^{10}
X	8658(78)	5147	8_0^{11}

TABLE 2. Experimental and calculated (ωB97X-2(LP)/6-311+G*) molecular properties of the neutral acetyl radical obtained in the present work, as well as comparison to available literature values. Reported vibrational frequencies correspond to the energy of the fundamental (v = 1) level relative to the zero-point energy.

Parameter	Expt.	Calc.	Lit.
EA, eV	0.4352(12)		0.423(37)[a]
ν_6, cm^{-1}	1046(3)	1072	
ν_7, cm^{-1}	834(2)	881	836.6[b]
ν_8, cm^{-1}	471(1)	472	468.1[b]

[a] Reference 16.

[b] Reference 19.

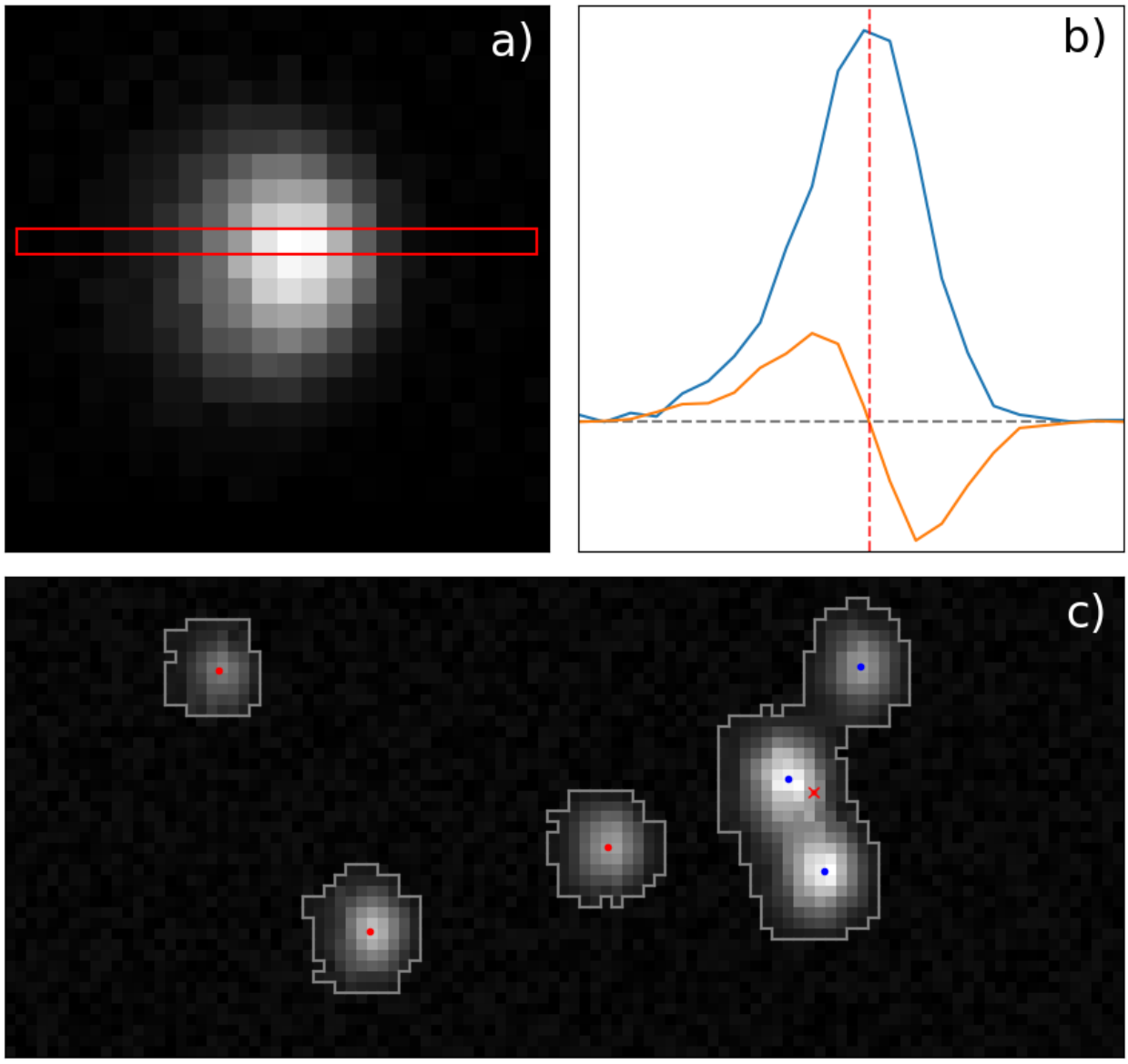

FIG. 1. Overview of the new centroiding algorithm presented in this work. (a) Illumination of phosphor screen from impact of photoelectron captured by CCD camera. Red bar highlights lineout of intensity plotted as a blue trace in the next panel. (b) Intensity through center of electron spot (blue) and the central finite difference of the intensity (orange) along the same axis. The red vertical line shows the center along the x-direction calculated with Eq. (1). (c) Centroids of electron spots determined with the new algorithm. The regions of connected bright (> 8% of maximum camera intensity) pixels are outlined in gray. Red dots are centroids of electron spots with sufficiently low pixel count, calculated using the CoM method. The red X shows the CoM centroid of the region of overlapping spots, which would have been rejected by the old method. Blue dots show centroids of the same region calculated with the new algorithm. All photoelectron spots shown are from detachment of OH^-.

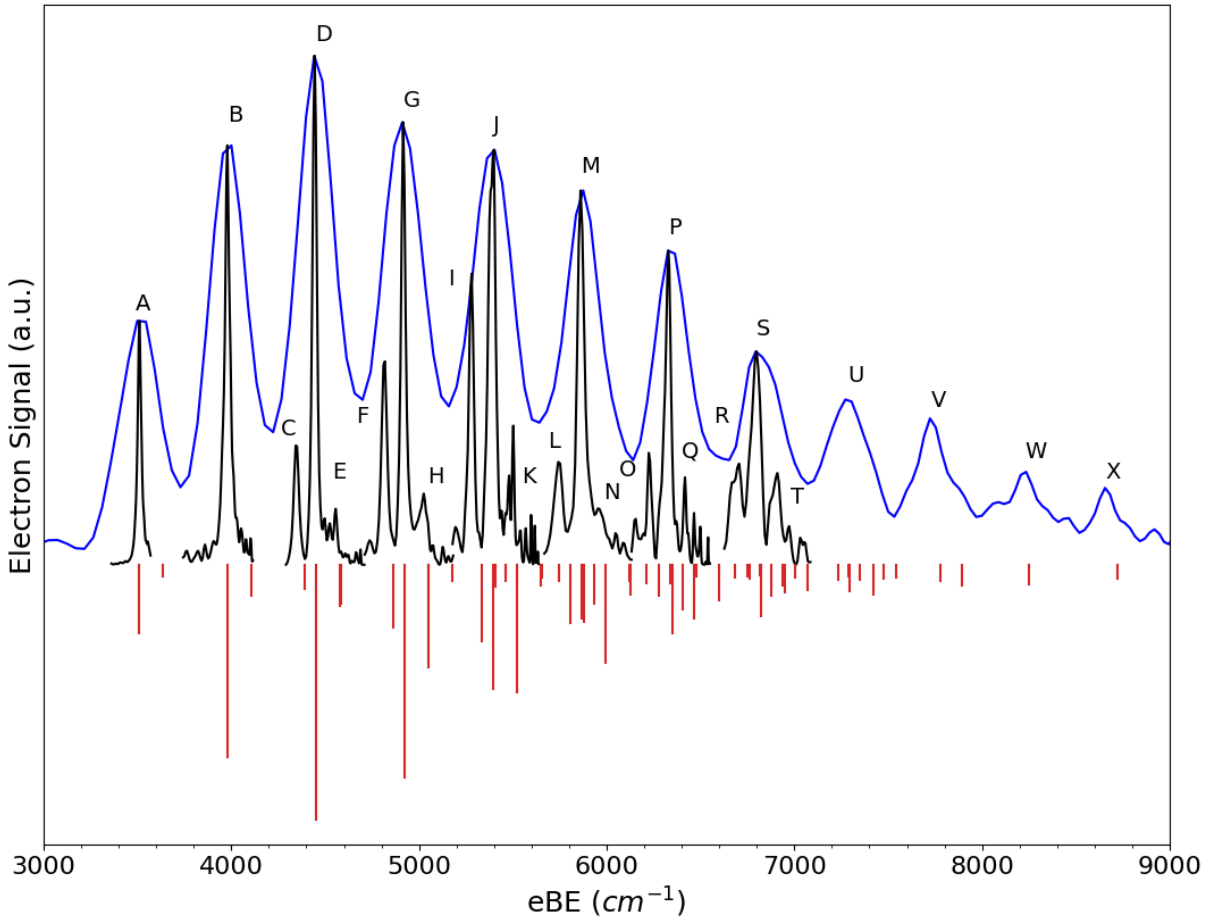

FIG. 2. Cryo-SEVI spectrum of the $\tilde{X}^2A' \leftarrow \tilde{X}^1A'$ detachment of acetyl, plotted as a function of electron binding energy (eBE). The blue trace is an overview spectrum taken at a high photon energy, and the black traces are high-resolution windows taken near threshold and scaled to match the intensities of the overview spectrum. The red stick spectrum is a Franck-Condon simulation based on ωB97X-2(LP)/6-311+G* results.

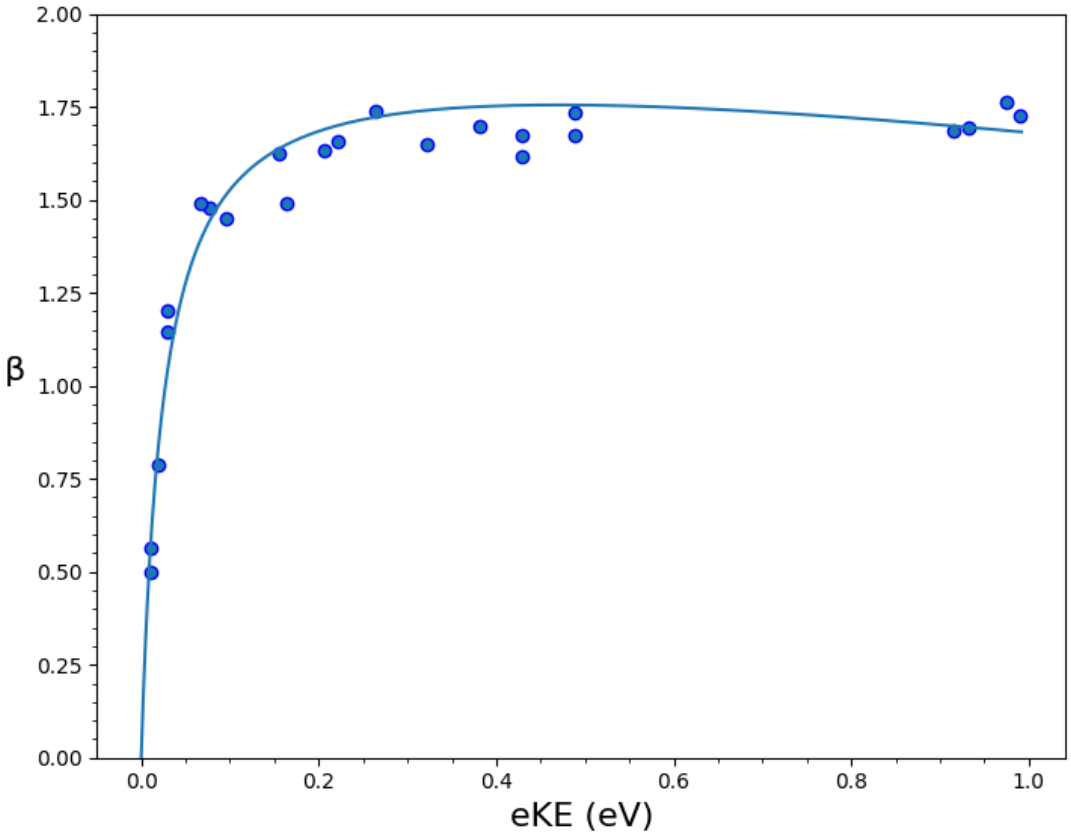

FIG. 3. Experimental PAD as a function of electron kinetic energy (eKE) calculated from the 0_0^0 and 8_0^1 transitions, as well as the fit to the mixed-*spd* model.

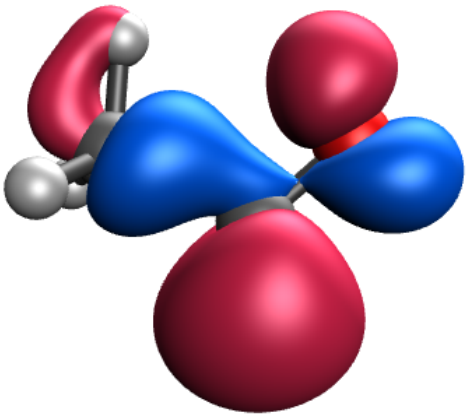

FIG. 4. Highest occupied molecular orbital of the acetyl anion calculated at the ωB97X-2(LP)/6-311+G* level of theory.

TOC Graphic: